Journal Pre-proofs

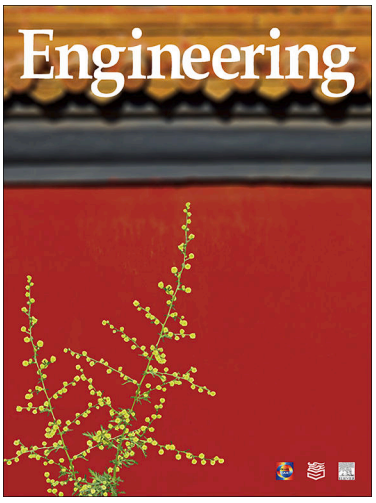

Article

A Hierarchical Molecular Encapsulation Strategy for Sustainable High-Performance Organic Solvent Nanofiltration Membranes

Mei-Ling Liu, Zhong-Hui Lin, An-Kang Li, Nadhita Chanchaona, Ming-Jian Tang, Zheng-Jun Fu, Cher Hon Lau, Shi-Peng Sun, Weihong Xing

PII: S2095-8099(26)00258-4
DOI: https://doi.org/10.1016/j.eng.2026.04.015
Reference: ENG 2336

To appear in: *Engineering*

Received Date: 12 November 2025
Revised Date: 26 February 2026
Accepted Date: 17 April 2026

Please cite this article as: M-L. Liu, Z-H. Lin, A-K. Li, N. Chanchaona, M-J. Tang, Z-J. Fu, C.H. Lau, S-P. Sun, W. Xing, A Hierarchical Molecular Encapsulation Strategy for Sustainable High-Performance Organic Solvent Nanofiltration Membranes, *Engineering* (2026), doi: https://doi.org/10.1016/j.eng.2026.04.015

A Hierarchical Molecular Encapsulation Strategy for Sustainable High-Performance Organic Solvent Nanofiltration Membranes

Mei-Ling Liu [a,b], Zhong-Hui Lin [a], An-Kang Li [a], Nadhita Chanchaona [c], Ming-Jian Tang [a], Zheng-Jun Fu [b], Cher Hon Lau [d], Shi-Peng Sun [a,b,e,*], Weihong Xing [a,e,*]

[a] *State Key Laboratory of Materials-Oriented Chemical Engineering, College of Chemical Engineering, Suzhou Future Membrane Technology Innovation Center, Nanjing Tech University, Nanjing 211816, China*

[b] *Nanjing Weihua Membrane Technology Co., Ltd., Nanjing 211800, China*

[c] *National Metal and Materials Technology Center (MTEC), National Sciences and Technology Development Agency (NSTDA), 114 Thailand Science Park, Klong Luang, Pathumthani 12120, Thailand*

[d] *School of Engineering, The University of Edinburgh, Edinburgh EH9 3JL, UK*

[e] *Suzhou National Laboratory, Suzhou 215100, China*

*Corresponding authors.
E-mail addresses: ssp@njtech.edu.cn (S.-P. Sun), xingwh@njtech.edu.cn (W. Xing)

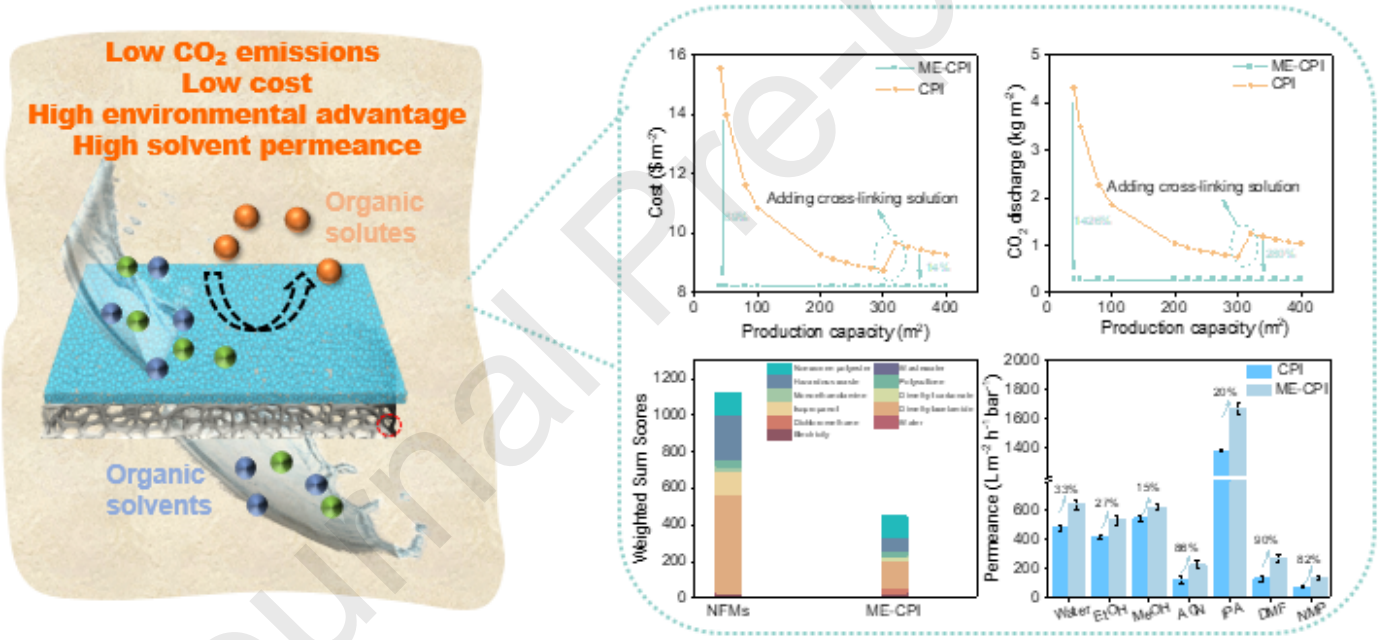

Highlights：

- Higher performance OSN membrane was prepared in a greener route by a hierarchical molecular encapsulation (HME) strategy.
- By encapsulation-release of nanocapsules, *in-situ* cross-linked substrate was constructed with 10-fold lower CO_2 emissions and 90% higher dimethylformamide permeace.
- Through cucurbit[6]uril-mediated host-guest chemistry, a highly permselective layer was formed exhibiting efficient separation for APIs solutions (>400 Da).

Abstract

Organic solvent nanofiltration (OSN) is pivotal for sustainable chemical separations, yet conventional membrane fabrication suffers from excess solvent consumption, environmental burdens, and performance trade-offs. Here, we present a hierarchical molecular encapsulation (HME) strategy that synergistically integrates protective-group chemistry and host-guest interactions to significantly advance OSN membrane production. By encapsulating cross-linkers within Boc-based nanocapsules for *in situ* release during phase inversion, this approach eliminates prolonged solvent immersion and intermittent replenishment while reducing cross-linking solution usage by 89%. The resulting solvent-resistant substrates feature rapid transport channels, enabling 90% higher dimethylformamide permeance than traditional methods. Concurrently, cucurbit[6]uril (CB[6])-mediated host-guest chemistry is used to engineer the selective layer's sub-nanometer pore structure, doubling the solvent permeability while maintaining >90% rejection of molecules larger than 400 Da. A demonstration of 1 m industrial-scale continuous production reveals an 89% reduction in module costs and 10-fold lower CO_2 emissions (validated via life-cycle assessment), with stable performance over 30 days. This work establishes a sustainable, scalable platform for industrial solvent recovery that resolves critical environmental and economic challenges.

Keywords Molecular encapsulation; Cross-linking; Fast solvent-transport channels; Organic solvent nanofiltration; Polyimide

1. Introduction

The extensive consumption of organic solvents in the chemical, pharmaceutical, and electronics industries has precipitated escalating environmental and economic burdens through the discharge of organic waste streams [1 – 5]. Advancing sustainable separation technologies for organic media is thus imperative. Organic solvent nanofiltration (OSN) has emerged as an energy-efficient solution for molecular-scale separations [6 – 12], yet its industrial implementation remains constrained by the inherent limitations of conventional membrane fabrication. State-of-the-art OSN membranes predominantly rely on a crosslinked polyimide (PI) [13 – 15] substrate fabricated via a three-step process involving solution preparation, phase inversion, and post-cross-linking [16]. While post-cross-linking increases solvent stability [17], this approach suffers from critical limitations: ① Excessive solvent consumption is required during prolonged immersion (typically 6–48 h) [18], which increases the already-high equipment and operational costs while contributing to significant environmental burdens; ② ensuring an adequate degree of substrate cross-linking necessitates excess reagent and intermittent replenishment [19,20]; and ③ solvent permeability is compromised due to reduced inter-chain spacing from covalent cross-linking [21,22]. These intertwined trade-offs among performance, sustainability, and scalability fundamentally hinder the industrial adoption of OSN.

Molecular encapsulation is an emerging technique that involves the incorporation of molecules into another molecule or material through physical or chemical means, resulting in the formation of stable encapsulated entities [23,24]. Importantly, the encapsulated molecules can be released in a controlled manner upon external stimulation, offering adaptability tailored to the specific application requirements [25 – 27]. In membrane science, preliminary efforts have explored the host-guest effect of cucurbit[n]uril-mediated amine diffusion [28,29] and di-tert-butyl decarbonate (Boc)-protected amine release for regulating the pore, charge, and surface patterns of water-treatment membranes [30,31]. However, the extension of these strategies to solvent-resistant membranes remains unexplored, primarily due to the challenge of synchronizing cross-linking and nanostructuring through the release of encapsulated agents.

Here, we bridge this gap by using a hierarchical molecular encapsulation (HME) strategy to fabricate high-performance polyamide OSN membranes (HME – PA). This approach synergistically integrates greener substrate engineering with high perm-selective thin-selective-layer optimization (Fig. 1). For the substrate, we introduce protection-group chemistry to encapsulate polyethyleneimine (PEI) cross-linkers within Boc-based nanocapsules. Unlike the conventional phase inversion + post-cross-linking method, these nanocapsules can be preloaded into the casting solution. Crucially, Boc protection prevents premature reaction during processing. During vapor-induced phase inversion, steam-triggered nanocapsule disintegration releases the PEI, enabling *in situ* cross-linking with PI. This novel methodology features two transformative advantages over conventional processes: ① Precise stoichiometric control eliminates cross-linker excess, reducing chemical consumption by 89% and avoiding the need for intermittent replenishment; and ② synchronizing the pore formation and cross-linking under steam exposure yields solvent-resistant substrates with vertically aligned nanochannels for rapid transport—a paradigm shift that replaces the resource-intensive phase inversion + post-cross-linking sequence with a sustainable single-step alternative.

To further improve perm-selectivity, we engineer the selective layer via host-guest complexation between cucurbit[6]uril (CB[6]) and piperazine (PIP). The CB[6]-PIP complex confines the interfacial polymerization (IP) to the surface, suppressing pore penetration and forming ultra-thin, highly permeable films. This coordinated substrate/selective-layer optimization creates ultra-fast solvent-transport pathways. Industrial-scale validation (1 m continuous production) confirms an 89% cost reduction and 10-fold lower carbon dioxide (CO_2) emissions, validated by life-cycle assessment (LCA). The resulting membranes exhibit higher perm-selectivity than state-of-the-art OSN membranes. This work establishes a scalable platform for sustainable membrane fabrication, benefiting precise separations in the pharmaceutical and petrochemical industries.

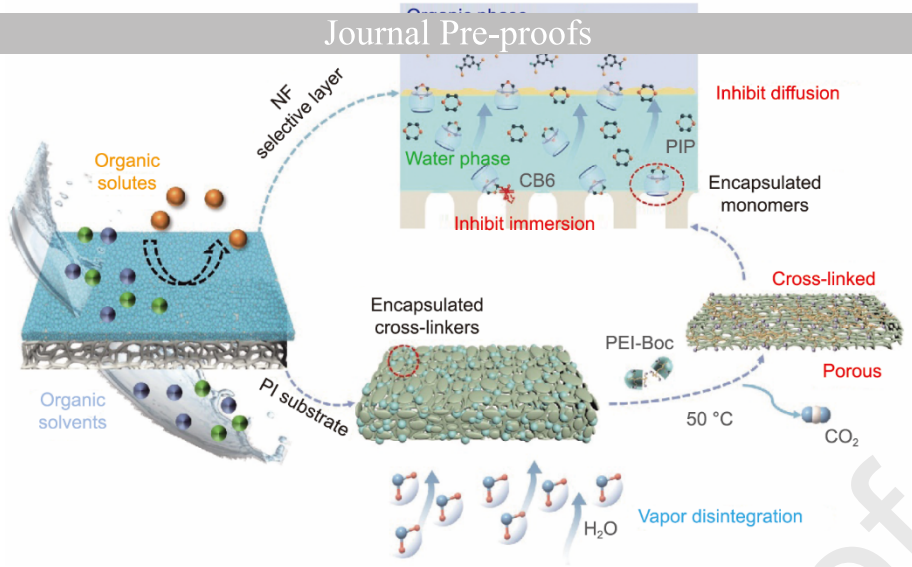

Fig. 1. Schematic diagram of the hierarchical molecular encapsulation strategy.

2. Material and methods

2.1. Materials

Polymer P84 (PI) was obtained from Vantico Inc., USA. Polyethyleneimine 600 (PEI600, 99%), Di-tert-butyl dicarbonate (Boc ,99%), 1,3,5-benzene tricarbonyl chloride (TMC, 98%), PIP (99%), CB[6], acetonitrile (ACN, 99%), *n*-hexane (98%), tetrahydrofuran (THF, 99%), rhodamine B (RB, molecular weight (M_W) = 778 g • mol^{-1}), malachite green (MG, M_W = 653 g • mol^{-1}), Janus green B (JGB, M_W = 511 g • mol^{-1}), congo red (CR, M_W = 697 g • mol^{-1}), polyethylene glycol (PEG) with various molecular weights (400, 1000, 2000, 10 000, 20 000, and 70 000 g • mol^{-1}; 99%), and active pharmaceutical ingredients (APIs) including curcumin (M_W = 368 g • mol^{-1}), tetracycline (M_W = 444 g • • mol^{-1}), roxithromycin (M_W = 837 g • mol^{-1}), and vitamin B12 (M_W = 1355 g • mol^{-1}) were purchased from Aladdin (USA). Dichloromethane (DCM, 99%) was purchased from Shanghai Ling Feng Chemical Reagents Co., Ltd., China. *N*, *N*-Dimethylacetamide (DMAc, 99.8%), *N*-methylpyrrolidone (NMP, 99%), isopropanol (IPA, 99.5%), dimethyl sulfoxide (DMSO, 99%), *N*, *N*-dimethylformamide (DMF, 99%), malachite green oxalate (MGO, M_W = 927 g • mol^{-1}), and brilliant blue R (BBR, M_W = 825 g • mol^{-1}) were sourced from Macklin (China). Acid fuchsine (AF, M_W = 585 g • mol^{-1}) was purchased from Adamas-beta (China). Methanol (MeOH, 99%), ethanol (EtOH, 99%), indigo carmine (IC, M_W = 466 g • mol^{-1}), crystal violet (CV, M_W = 407 g • mol^{-1}), and methyl orange (MO, M_W = 327 g • mol^{-1}) were purchased from Sinopharm Chemical Reagent Co., Ltd., China. All the chemicals and reagents listed above were used directly without further purification.

2.2. Preparation of HME nanofiltration membranes

To prepare the molecular encapsulation cross-linked PI (ME-CPI) substrate, PEI-Boc nanocapsules (at concentrations of 16, 18, 22, and 25 wt%) were added to DMAc and mixed for 8 h at 40 ° C to achieve uniform dispersion. Next, 16 wt% PI particles were added to the solution, and the mixture was stirred continuously to form a homogeneous dope solution, which was then left at room temperature for 24 h to remove bubbles. The dope was subsequently cast onto polyester nonwoven fabric using a 300 μm scraper, then immersed in deionized water for 1 min to induce phase transformation. The resulting substrate containing PEI-Boc nanocapsules was designated as ME-PI. This substrate was then placed in a 50 °C steam environment to facilitate Boc removal and PEI release. The steam environment was maintained using a temperature-controlled water bath at 50 °C with 95% relative humidity, achieving a water vapor pressure of 11.685 * 10^3 Pa. This process led to cross-linking between the PEI and PI. Finally, the ME-CPI was rinsed and stored in deionized water, and the synthesis was verified by means of ^{13}C nuclear magnetic resonance (Fig. S1 in Appendix A).

For comparison, a cross-linked polyimide substrate (CPI) was prepared using a conventional post-cross-linking method. PI particles (16 wt%) were added to DMAc solvent and stirred continuously to obtain a uniform casting solution, which was left at room temperature for 24 h to remove bubbles. The casting solution was then applied onto polyester nonwoven fabric using a 300 μm scraper and immersed in deionized water to induce phase transformation. The substrate was soaked in 5 wt% PEI600 (in IPA) for 6 h for cross-linking. After cross-linking, the substrate was removed and placed in deionized water for 12 h for solvent exchange. The CPI substrate was stored in deionized water for further use.

Three types of IP were conducted on the ME-CPI substrate to prepare polyamide composite nanofiltration membranes. The first method, conventional IP, involved immersing the substrate in a 0.1 wt% PIP aqueous solution for 2 min. After removing

excess monomers with a soft rubber roller, the top surface of the substrate was immersed in a 0.1 wt% TMC/*n*-hexane solution for the substrate in a 0.1 wt% TMC/*n*-hexane solution for 1 min, followed by drying. The substrate was then coated with a 0.1 wt% PIP aqueous solution for 2 min. Finally, the dried substrate was immersed again in the 0.1 wt% TMC/*n*-hexane solution for 1 min, and excess *n*-hexane was removed. The composite polyamide membrane resulting from the dual-step IP was designated as DPA. The third method was carried out using the water-phase/oil-phase method, with an aqueous solution containing 0.1 wt% PIP and 0.05 wt% CB[6] at pH 6.5 and an n-hexane solution with 0.1 wt% TMC. The resultant membrane, regulated by HME in both the selective layer and substrate, was labeled as HME-PA. The CPI-PA membrane employs the same selection layer as the HME-PA membrane, but its substrate is composed of CPI. Successful synthesis of the selection layers for the HME-PA, PA, and DPA membranes was confirmed by means of Fourier-transform infrared (FTIR) characterization (Fig. S2 in Appendix A).

2.3. Membrane characterization

The chemical structure of the membranes was confirmed using FTIR (Thermo Nicolet8700, USA). The chemical composition of the membrane surface was analyzed using X-ray photoelectron spectroscopy (XPS; Thermo Scientific KAlpha, USA). Nuclear magnetic resonance (NMR; Bruker AVII 400 MHz, USA) was used to characterize the chemical structure of PEI-Boc. ^{13}C NMR measurements were performed on a Bruker Avance Neo 400WB spectrometer operating at 100 MHz (^{13}C) using the magic angle spinning (MAS) technique. The film was ground to powder in order to fit efficiently into the 3.2 mm MAS rotor, so the maximum speed of magic angle spinning was 10 kHz. ^{13}C cross-polarized MAS sequences were used. The average particle size of the PEI-Boc was characterized using a nanoparticle size and zeta potential analyzer (Zeta Sizer Nano-ZS90, UK). Field-emission scanning electron microscopy (FE-SEM, Hitachi S4800, Japan) was used to observe the surface and cross-sectional morphology of the membranes. To characterize changes in amine content, the ME-PI and ME-CPI substrates were immersed in a 200 ppm $CuCl_2$ solution for 5 min or 24 h, and the distribution of Cu^{2+} captured by amine groups before and after Boc degradation was observed using energy-dispersive X-ray spectroscopy (EDX; Hitachi S4800, Japan). The transverse relaxation time (T_2) of molecules in the nanopores was measured by means of a low-field nuclear magnetic resonance (LF-NMR) imaging analyzer (NM42-40H-I, China), with ethanol used to probe the nanopores within the membranes. A zeta electric analysis meter (SurPASS3, Anton Paar, Austria) and a rheometer (AR-G2 rheometer, TA instruments, USA) were utilized to analyze the membrane surface charge and the viscosity changes of the dope solution, respectively.

2.4. Synthesis of PEI-Boc nanocapsules

Boc and PEI600 were dissolved in DCM according at a mass ratio of 2.08:1. The Boc solution was then slowly added to the PEI600 solution, and the mixture was stirred at room temperature for 12 h to ensure a complete reaction. After the reaction, a milky white dispersion formed, which was collected by centrifugation at 10 000 r • min^{-1}. The resulting product—pure white PEI-Boc nanocapsules—was obtained after washing with DMAc. The ^1H-NMR (D_2O) spectrum showed characteristic signals at δ 5.44 (d, 1H), 3.48 (s, 3H), 3.29 (s, 5H), 3.03 (s, 14H), 2.88 (s, 9H), 2.78 (s, 16H), 2.68 (s, 19H), 1.44 (d, 18H), and 1.23 (s, 2H) ppm.

2.5. Characterization of mechanical properties

The mechanical properties of the membranes were tested using an electromechanical universal testing machine (Tian Yuan, TY8000, China). Samples were cut into 3 mm strips. The data presented represent the average values obtained from three separate tests. Tensile stress and strain were calculated using the following formulas:

$$\sigma = \frac{F_b}{S_0} (1)$$

$$\varepsilon = \frac{H - H_0}{H_0} (2)$$

where σ is the tensile strength or tensile stress of the membrane (mPa), F_b is the applied tensile force (N), S_0 is the cross-sectional area of the substrate (mm^2), and H_0 and H are the initial and fracture limit lengths of the substrates (mm), respectively.

2.6. Solvent-resistance test

To investigate the solvent resistance of the ME-CPI substrate, the weight loss ratio (W, %) of the substrate in different organic solvents was calculated. First, a certain mass of the substrate was weighed after thorough drying. Then, it was

immersed in various organic solvents, including EtOH, IPA, ACN, DMF, and NMP, for 48 h. Next, the samples were placed in dsing the following formula:

$$W = (1 - \frac{M}{M_0}) \times (3)$$

where M_0 (g) and M (g) are the dry weights of the ME-CPI substrate before and after immersion in various solvents, respectively.

2.7. Characterization of pore size distribution

The molecular weight cut-offs (MWCOs) of the membranes were measured using 200 ppm PEG aqueous solutions with molecular weights of 400, 800, 1000, 2000, 10 000, 20 000, and 70 000 Da. The concentrations in the permeate and feed were analyzed using a total organic carbon analyzer (TOC-VCPH; Shimadzu, Japan). The specific calculation method has been detailed previously [32]. The MWCO was determined when the rejection rate (R) reached 90%.

2.8. Evaluation of nanofiltration performance

The solvent-permeance and rejection performance of the membranes was evaluated using a dead-end filtration apparatus. The evaluation system included various pure organic solvents and 200 ppm dye and 25 ppm API solutions in methanol. Before testing, the membranes were compacted for 30 min at 10 bar to achieve a steady performance. The permeance (Perm, L • m^{-2} • h^{-1} • • bar^{-1}) and rejection rate (Rej, %) were calculated using the following equations:

$$\mathrm{Perm} = \frac{\Delta \mathrm{m}}{\mathrm{A} \times \mathrm{t} \times \Delta \mathrm{P} \times \rho} (4)$$

$$\mathrm{Rej} = (1 - \frac{\mathrm{C_p}}{\mathrm{C_f}}) \times 100\% (5)$$

where Δm (kg) is the mass of solvent permeated within a certain time, A is the effective filtration area (3.14 * 10^{-4} m^2), t is the testing time (h), ΔP is the transmembrane pressure (10 bar), and ρ is the solvent density (kg • • m^{-3}). C_p and C_f are the solute concentrations on the permeate and feed sides, respectively, measured using an ultraviolet – visible (UV – Vis) light spectrophotometer (UV2450, Shimadzu). Each condition was tested on more than three membranes, and the reported values represent the averages.

The long-term separation stability of the membrane in organic solvents was evaluated as follows. First, the initial rejection performance of the membrane for CR in methanol was tested using a crossflow filtration setup with a flow rate of 50 L • h^{-1}, a pressure of 8 bar, and an effective area of 7.07 * 10^{-4} m^2. Following this, the membrane module was immersed in NMP for 3 days after shutting down the device. This procedure was repeated for 30 days.

2.9. Environmental impact comparison of ME-CPI vs CPI fabrication procedures via LCA

The environmental impacts of the conventional fabrication process for CPI and our proposed approach for ME-CPI were evaluated using LCA, a widely adopted quantitative assessment method [33]. This LCA followed the ISO 14040 and 14044 standards [34,35]. The goal of this assessment was to verify the hypothesis that ME-CPI fabrication would have lower environmental impacts. The comparison used a functional unit of 100 m^2 of membrane produced. The system boundary spanned from cradle to gate, covering raw material acquisition, lab-scale fabrication, and waste disposal from the fabrication stage. The system was initially intended to reflect the conditions in Nanjing, China—the actual laboratory location. However, due to limited region-specific data in the ecoinvent v3 database, average global datasets were used, with the exception of the electricity grid mix, which was specified for the East China grid. Inventory tables for both the ME-CPI and CPI fabrication processes are provided in Table S1 in Appendix A. Proxy data were employed for certain unavailable compounds, including PI, PEI600, and Boc; justification for these proxies is provided in Table S2 in Appendix A. The chosen calculation method was IMPACT WORLD + Endpoint v1.47 [36], covering 27 impact categories including both short- and long-term environmental effects. These impacts were weighed using Stepwise 2006 [37], aggregated, and reported as a single monetized score in EURO2003. The LCA analysis was conducted using Simapro software (the Netherlands).

3. Results and discussion

3.1. Molecular encapsulation for substrate structure construction

To construct solvent-resistant substrates with enhanced transport properties, we employed a molecular encapsulation strategy. The primary amine groups in PEI were Boc-protected to form PEI-Boc nanocapsules, and their successful synthesis was verified using ^{1}H NMR (Fig. S3 in Appendix A). The PEI-Boc was pre-doped into the PI casting solution (Fig. 2(a)). Following a brief phase-inversion step in water, the nascent membrane (designated as ME-PI) was exposed to hot steam. Under high-temperature and high-humidity conditions, water vapor permeates into the interior of the nanocapsules, increasing the molecular mobility. This drives the hydrolysis of the tert-butylamide bonds, accompanied by the release of CO_2 and tert-butanol, while simultaneously regenerating the PEI primary amine groups. The PEI amine groups subsequently cross-linked *in situ* with the PI chains to form the ME-CPI substrate. We analyzed the encapsulation and release processes using EDX and XPS. Amine groups exhibit a strong ability to adsorb heavy metal ions [38]. Here, Cu^{2+} ions were used as indicators. EDX mapping of the copper (Cu) distributions on the ME-PI and ME-CPI substrates after immersion in $CuCl_2$ solution (Fig. 2(b–e)) revealed minimal Cu adsorption**,** comparable to that observed before the Boc degradation (5 min vs. 24 h immersion). This result indirectly reflects the distribution and state of the PEI-Boc nanocapsules within the substrate. As shown in Figs. 2(b) and (c), only minimal Cu ion adsorption was observed on the substrate surface, and there was little difference between the 5-min and 24-h levels before Boc degradation, suggesting that the amines were effectively protected. The ME-PI substrate exhibited particulate matter with an approximate diameter of 100 nm, slightly larger than the free PEI-Boc nanocapsules (~80 nm, Fig. 2(f)), indicating nanocapsule aggregation within the substrate.

In contrast, after the hot-steam-induced Boc degradation (forming ME-CPI), a significant increase in uniformly distributed Cu adsorption sites was observed (Figs. 2(d) and (e)), confirming the controlled release and exposure of primary amines. XPS analysis of the nitrogen species (Fig. S4 in Appendix A) further elucidated this process. In the ME-PI (pre-degradation), the spectrum reflected contributions from tertiary/secondary amines in the PEI, encapsulated primary amines, and tertiary amines in the PI. The N/O ratio increased in comparison with pure PI (Fig. 2(g)), primarily due to exposed secondary/tertiary amines from PEI. Following Boc degradation (ME-CPI), a substantial rise in primary amines and a corresponding decrease in secondary amines (indicating the consumption of imide groups via cross-linking) were evident, leading to a further increase in the N/O ratio. FTIR analysis further confirmed the degradation of PEI-Boc and the successful cross-linking of PI. The FTIR spectra of the ME-CPI substrate, compared with those of the PI and ME-PI substrate (Fig. S5 in Appendix A), revealed new peaks at 1649 cm^{-1} (C=O) and 1540 cm^{-1} (C–N); these characteristics of amide bond formation [39] signified the successful incorporation of PEI and *in situ* cross-linking with PI. Concomitantly, a noticeable reduction in the intensity of the imide characteristic peaks at 1722 cm^{-1} (C=O) and 1363 cm^{-1} (C–N) was observed, further supporting the chemical transformation of the substrate.

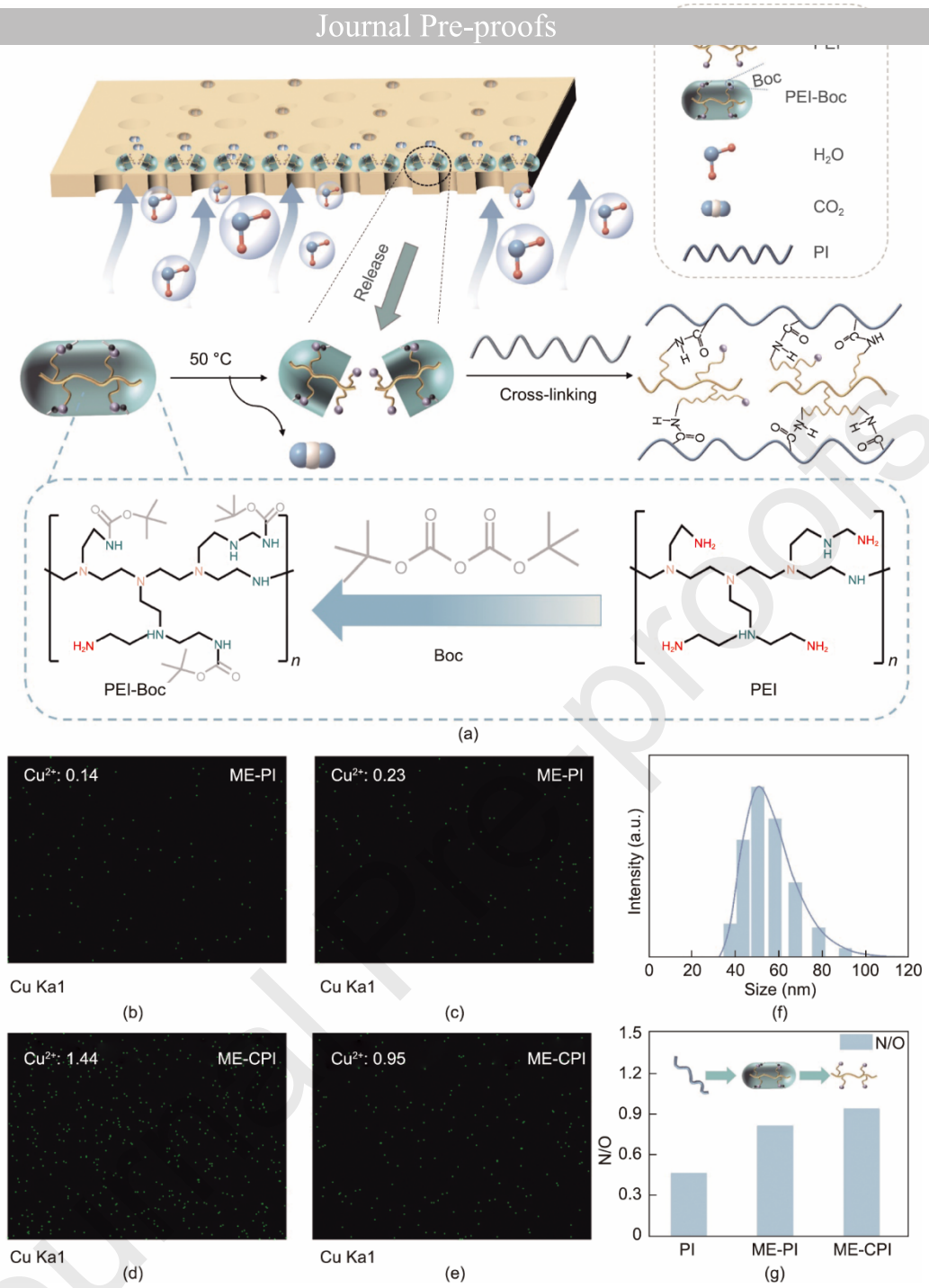

Fig. 2. Encapsulation and release process of PEI-Boc nanocapsules. (a) Schematic diagram of the release process of PEI-Boc; (b, c) copper elemental distributions (green dots) measured by EDX on the top surface of the ME-PI substrates after immersion in $CuCl_2$ solution for 5 min and 24 h, respectively; (d, e) copper elemental distributions (green dots) measured by EDX on the top surface of the ME-CPI substrates after immersion in $CuCl_2$ solution for 5 min and 24 h, respectively; (f) size distribution of the PEI-Boc nanocapsules; (g) N/O ratio of the PI, ME-PI, and ME-CPI substrate.

The degree of cross-linking, governed by the PEI-Boc content, directly impacted the solvent resistance. The weight loss ratio of the ME-CPI substrates in NMP decreased from 7.09% (16 wt% PEI-Boc) to 1.68% (25 wt% PEI-Boc) (Fig. S6 in Appendix A), confirming improved solvent resistance with higher cross-linker loading. However, incorporating 25 wt% PEI-Boc significantly increased the dope solution viscosity (Fig. S7 in Appendix A), hindering uniform casting and resulting in defective substrates (Fig. S8 in Appendix A). Consequently, the study focused on 22 wt% PEI-Boc for subsequent experiments. The ME-CPI substrates (22 wt% PEI-Boc) exhibited superior solvent resistance compared with both the pristine PI and the conventionally post-cross-linked CPI substrates across a range of polar and non-polar solvents (Fig. 3(a); Fig. S9 in Appendix A). This increased stability stems from the robust covalent cross-links formed *in situ* by the released PEI600. Furthermore, the steam treatment duration modulated the solvent tolerance, with short exposures being sufficient for stability in alcohols

and acetonitrile (Fig. S10 in Appendix A). This finding supports the feasibility of the continuous fabrication of ME-CPI subs[Journal Pre-proofs]olar aprotic solvents, such as NMP, providing versatility for subsequent applications in a variety of solvent systems.

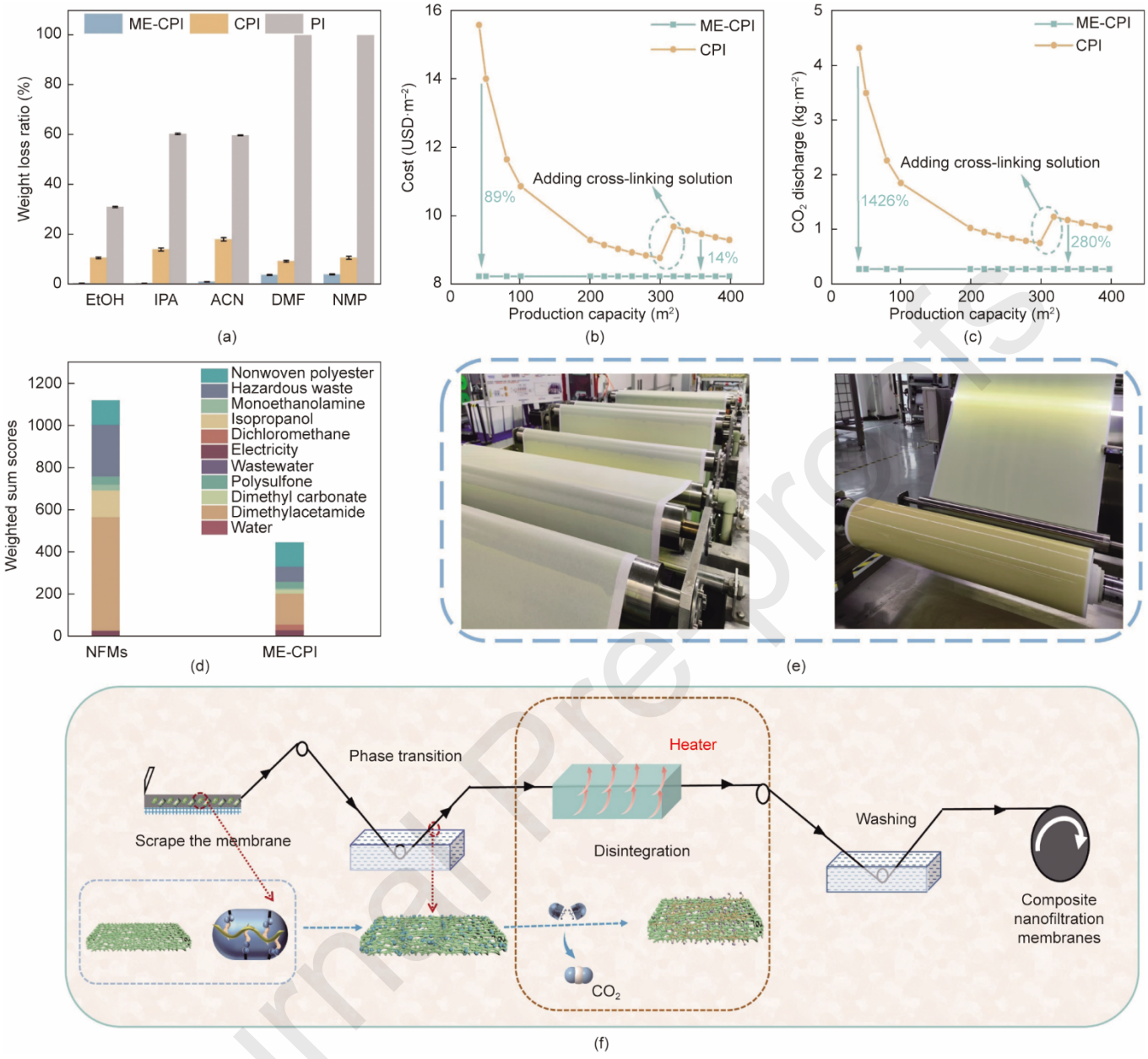

Fig. 3. Cross-linking of PI substrate. (a) Weight loss ratio of ME-CPI, CPI, and PI substrates in various solvents; (b) cost of producing ME-CPI and CPI substrates with different surface areas; (c) CO_2 emissions from producing ME-CPI and CPI substrates with different surface areas; (d) total environmental impact weighted scores for the ME-CPI and CPI fabrication processes, with each bar segmented to show contributions from individual input or output components; (e) a 1-m-wide production line based on the ME-CPI substrate; (f) schematic diagram of continuous production of the substrates.

A comprehensive cost and environmental impact analysis was performed, comparing the ME-CPI and CPI substrates (Figs. 3(b) and (c); Table S3 in Appendix A). The fabrication of CPI-based membranes using conventional post-cross-linking methods requires an excessive amount of cross-linker and solvents, incurring high costs; it also generates significant CO_2 emissions, primarily from IPA post-treatment. Furthermore, during the production process, the variation in cross-linker concentration necessitates intermittent replenishment, making it challenging to precisely control membrane performance and achieve continuous production. In contrast, the molecular encapsulation strategy employed to fabricate the ME-CPI-based substrates incorporates a predetermined amount of cross-linker directly into the casting solution, coupled with thermal-vapor-induced release. This approach addresses the issues of excessive cross-linker and solvent use, thereby reducing both costs and environmental impact. It enables accurate cost prediction and allows for the preemptive estimation of continuous production costs based on production capacity. The cost remains stable over production capacity, and both the cost and CO_2 emissions are significantly lower than those for CPI-based membranes. Using a standard 8040-membrane module (~38 m² effective area), the ME-CPI substrate demonstrated significant advantages in both cost and environmental impact: The cost per module

decreased by an impressive 89% (Fig. 3(b)), while CO_2 emissions were reduced by 10-fold (1426%; Fig. 3(c)).

T[redacted]CPI fabrication process, as this process had a total impact weighted score approximately 2.5 times lower than that of CPI production. The omission of IPA, whose impact alone exceeds that of the entire ME-CPI process, was the primary driver. Although the proposed process is not yet fully green, replacing the most solvent-intensive step represents a significant advancement toward sustainable OSN membrane production. Critically, scale-up feasibility was demonstrated by the stable continuous production of ME-CPI substrates on a 1-m-wide production line (Figs. 3(e) and (f)).

3.2. Properties and performance of ME-CPI substrate

The microstructural evolution induced by the incorporation of PEI-Boc was systematically investigated. Importantly, the CO_2 released during Boc degradation acted as a pore-forming agent, diffusing through the polymer matrix and reshaping the substrate's pore architecture. Surface scanning electron microscopy (SEM) analysis revealed a transition from a non-porous morphology in ME-PI (pre-degradation, Fig. 4(a)) to a uniformly microporous surface in ME-CPI (post-degradation, Fig. 4(b)). This finding confirmed the pore-generating effect of Boc decomposition, concurrent with the disappearance of the white PEI-Boc nanocapsules.

Cross-sectional SEM further demonstrated significant structural differences (Fig. 4(c) and Fig. S12 in Appendix A): While the pristine PI substrates exhibited dense, micron-sized pores, the ME-CPI substrates developed vertically aligned macrovoids penetrating the entire structure. This transformation is attributed to two synergistic effects of PEI-Boc:

(1) Viscosity modulation. The PEI-Boc increased the dope solution viscosity (Fig. 4(d)), elevating the critical solvent concentration required for phase separation. This suppresses the nucleation of small pores while slowing macrovoid growth [40].

(2) Accelerated solvent exchange. The mild hydrophilicity of the PEI-Boc accelerates solvent-nonsolvent interdiffusion in the polymer-lean phase, shortening the delayed phase-separation time. The resultant low polymer concentration at the onset of phase separation favors the growth of straight through-pores (Fig. 4(c)).

Increasing the PEI-Boc content progressively eliminated the small, non-continuous finger-like pores in the sublayer (Figs. S13 and S14 in Appendix A), and substrates with high PEI-Boc concentrations exclusively featured straight, finger-like through-pores. The latter structure facilitates faster solvent transport and endows the substrate with excellent solvent resistance and permeance (Fig. S15 in Appendix A). Notably, compared with that of the CPI substrates prepared using the traditional method, the solvent permeance of the ME-CPI substrate increased by over 20%, with its DMF permeance increasing by 90% (Fig. 4(e)).

LF-NMR was used to probe the solvent-transport dynamics in the pore networks (Fig. 4(f)). Both ME-CPI and CPI showed broad T_2 distributions (10^{-1}–10^3 ms), indicating surface-adsorbed ethanol molecules. Notably, ME-CPI exhibited a pronounced rightward shift of the T_2 peak within the nanoconfined regime (10–10^3 ms), signifying extended relaxation times. This finding evidences wider and less tortuous transport pathways [41], consistent with the observed improvement in permeance.

Mechanical strength is crucial for separation membranes. The regular, interconnected pore structure of the ME-CPI substrate leads to a uniform distribution of stress, conferring superior mechanical strength [42]. A tensile strength test confirmed that the ME-CPI substrate possessed significantly higher tensile strength than its CPI counterparts prepared via conventional post-cross-linking methods (Fig. 4(g)), highlighting the suitability of the ME-CPI substrate for industrial applications. The proposed process produced substrates with low solvent consumption, uniform cross-linking, high mechanical strength, and rapid transport channels, overcoming the limitations of conventional methods and providing a novel template for further thin-film coating, as discussed in the next section.

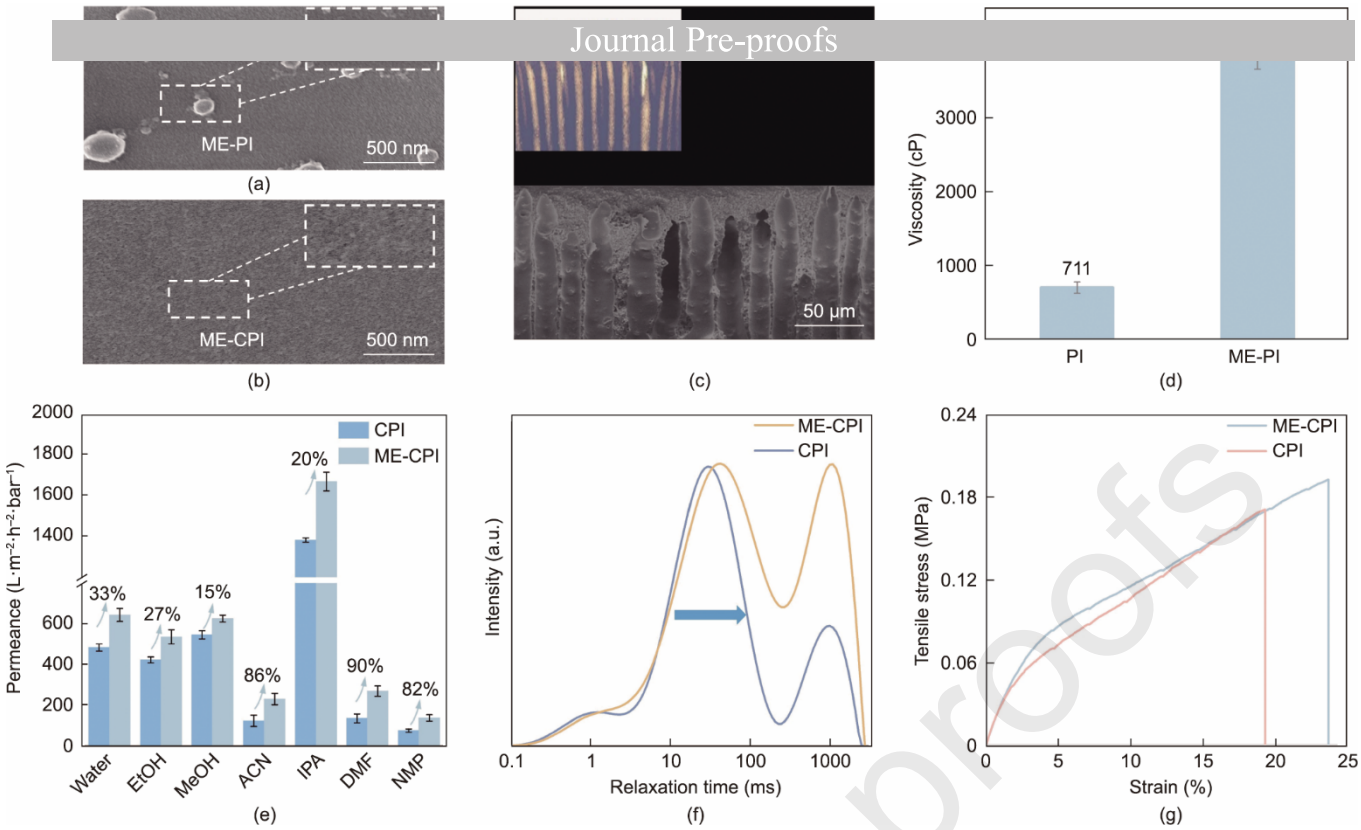

Fig. 4. Structural shaping of the ME-CPI substrate: (a, b) Surface SEM images of the (a) ME-PI and (b) ME-CPI substrates; (c) cross-sectional SEM image and optical microscope image of the ME-PI substrate; (d) viscosity of the PI and ME-PI dope solutions; (e) solvent permeance of the ME-CPI and CPI substrates; (f) ^{1}H time-domain NMR spectra of the ME-CPI and CPI substrates; (g) tensile stress-strain curves of the ME-CPI and CPI substrates.

3.3. Preparation and organic solvent nanofiltration performance of HME-PA composite membranes

The chemical and pharmaceutical industries demand sub-nanometer separation technologies for high-purity solvent recovery. Leveraging the ME-CPI substrate's fast mass-transport channels, robust solvent resistance, and high cross-linking density, we constructed thin-film composite (TFC) nanofiltration (NF) membranes via tailored IP (Figs. 5(a), S16, and S17 in Appendix A).

Initial attempts revealed that conventional single-step IP on the macroporous ME-CPI substrate led to monomer penetration into pores, causing pore blockage and reduced performance (Figs. 5(a) and (b)) [43]. To address this issue, a dual-step IP strategy was developed, involving ① the pre-reaction of residual amines from the *in situ* cross-linked PI with trimesoyl chloride (TMC), which reduces the pore sizes of the substrate (Fig. S18 in Appendix A), thus preventing monomer penetration; and ② subsequent PIP/TMC polymerization, which forms a dense selective layer. This approach yielded a DPA membrane with enhanced solvent permeance versus conventional PA. Specifically, the permeability of HME-PA membranes for methanol reaches 15.49 $L \cdot m^{-2} \cdot h^{-1} \cdot bar^{-1}$, more than double that of a conventional PA membrane (CPI-PA)(Figs. 5(a), (b), and S20 in AppendixA).

Further innovation integrated molecular encapsulation into the selective layer. By exploiting host-guest interactions between CB[6] and PIP, PIP monomers were encapsulated during IP (to form an HME-PA membrane). This strategy inhibited PIP diffusion into the substrate (Fig. 5(a)), ensuring surface-confined polymerization and forming an highly perm-selective layer in only one step (Figs. S17 and S19 in Appendix A). More specifically, CB[6] forms a host-guest complex with PIP, exhibiting a high binding affinity, thereby modulating the mass-transfer kinetics of PIP and facilitating the formation of a more uniform initial PA with fewer defects [44]. Furthermore, the negative charge on the ME-CPI substrate, combined with the negative charge of the CB[6] terminal carbonyl group and unreacted carboxyl groups (–COOH) within the PA network, may increase the stability between the selected layer and substrate. This is achieved through hydrated ions or the formation of hydrogen-bond networks with polar groups on the substrate surface [8,45,46]. Consequently, HME-PA exhibited near-doubled methanol permeance (vs PA) while maintaining comparable rejections. It is noteworthy that the permeance of the HME-PA, DPA, and PA membranes all significantly exceeded those of the membranes based on CPI substrates, directly confirming that the ME-CPI substrates possess outstanding capabilities for rapid solvent permeation (Figs. 5(b), S20, and S21 in Appendix A). Additionally, the hydrolysis of residual acyl chloride groups on the composite membrane surface after IP maintained the distinct negative charge characteristics of the membrane (Fig. S22 in Appendix A). Based on sub-nanometer pore screening and electrostatic interactions, the membrane demonstrated a retention rate exceeding 90% for negatively charged molecules with a molecular weight greater than 400 Da and up to 99.2% for BBR (825 Da, negatively charged) (Fig.

S21). It also exhibited moderate rejection capabilities for positively charged molecules with a molecular weight of 400–800 Da (

osite membranes improved, while the rejection remained constant (Fig. S24 in Appendix A). This finding further confirms that the straight, finger-like through-pores in the substrate facilitate rapid solvent transmission with low resistance. Compared with current state-of-the-art OSN membranes, the HME-PA membrane achieves a superior permeate selectivity trade-off while exhibiting a permeate flux exceeding that of the commercial Duramem 200 membrane by over 100% (Figs. S25 and S26; Tables S4 and S5 in Appendix A).

To investigate the potential applications of HME-PA membranes in the pharmaceutical field, we selected four drug molecules with distinct structures and functions for separation testing. The HME-PA membrane demonstrated excellent rejection performance for APIs with molecular weights greater than 400 Da (rejection: >90%), achieving a particularly high rejection of 99% for vitamin B12 (1355 Da) (Fig. 5(c)). Critically, the membrane maintained stable solute rejection over 30 days of continuous operation (Fig. 5(d)), demonstrating exceptional durability in organic solvents. This long-term operational stability indirectly corroborates the conclusion that the CB[6]-PIP complex is immobilized within the selective layer.

These results fully demonstrate the HME-PA membrane's significant application potential within the pharmaceutical industry for high-value organic solvent recovery and the efficient concentration of drug molecules. To evaluate the scalability of the HME technology, we fabricated HME-PA membranes with a width of 1 m. The uniformity of the membrane was tested using samples taken at different locations along one roll of the continuously produced substrate. The CR rejection and permeance data demonstrated that the HME technology possesses excellent scalability and substrate uniformity (Fig. 5(e)), providing decisive performance evidence for its industrial application. The HME strategy—applied to both the substrate (PEI-Boc) and the selective layer (CB[6]-PIP)—enables the elimination of multi-step substrate modification and precise pore-architecture control. This synergy delivers high-flux, high-selectivity OSN membranes with minimized environmental and economic footprints for fine chemical processes.

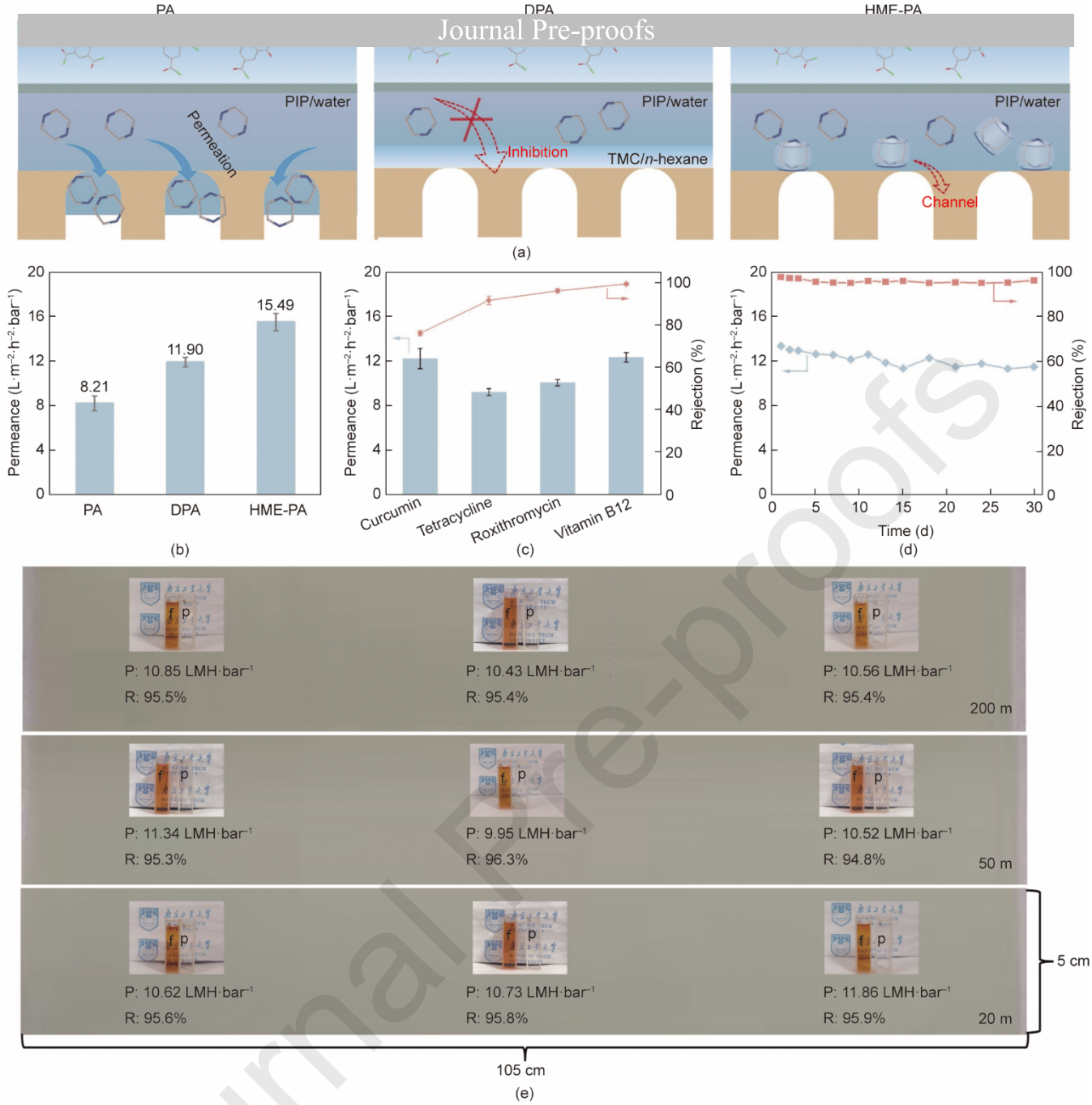

Fig. 5. Preparation and performance of HME-PA: (a) Schematic diagram of the interfacial polymerization process for the PA, DPA, and HME-PA membranes; (b) comparison of the methanol permeance of the PA, DPA, and HME-PA membranes; (c) permeance and rejection performance of the HME-PA membrane toward APIs in methanol; (d) long-term stability test of the HME-PA membrane in a methanol system; (e) evaluation of uniformity in the preparation of HME-PA membrane via IP on a large-area ME-CPI substrate (f, p, and LMH represent feed solution, permeate, and permeation flux ($L \cdot m^{-2} \cdot h^{-1}$), respectively.).

4. Conclusion

The HME strategy presented herein successfully resolves the long-standing trilemma involving sustainability, scalability, and performance in OSN membrane fabrication. Diverging fundamentally from conventional methods that rely on stochastic monomer diffusion after membrane solidification, the HME strategy leverages *in situ* nanocapsule decomposition during phase inversion to synchronize cross-linking with pore formation. This paradigm shift eliminates intermittent reagent replenishment, enables vertically aligned pore architectures, and resolves the bottleneck regarding the degree of cross-linking of the substrate in cross-linked PI membranes. The proposed approach achieves an 89% reduction in cross-linker consumption and a tenfold decrease in CO_2 emissions. Not only does this approach mark a significant breakthrough in the field of sustainable membrane manufacturing, but its universal design also offers a promising path for improving the performance of other separation membrane systems. Crucially, the synergistic design of a solvent-resistant substrate and a perm-selective layer demonstrates that molecular-level structural control can transcend the permeability–selectivity trade-off, doubling

solvent permeance while maintaining >90% rejection of solutes with molecular weights larger than 400 Da. By enabling the prec and environmentally benign molecular separations in pharmaceutical and chemical processing.

Conflict of interest statement

We honestly state that neither this manuscript nor its contents have been published previously, and we have no competing financial interests.

Acknowledgements

The authors gratefully acknowledge research funding provided by the National Natural Science Foundation of China (22378193, 22578198), the Jiangsu Science and Technology Department (BE2023808), the Basic Research Program of Jiangsu (BK20232010), and the Jiangsu Future Membrane Technology Innovation Center (BM2021804).

References

[1] Jiang Z, Dong R, Evans AM, Biere N, Ebrahim MA, Li S, et al. Aligned macrocycle pores in ultrathin films for accurate molecular sieving. Nature 2022;609(7925):58–64.
[2] Kang J, Ko Y, Kim JP, Kim JY, Kim J, Kwon O, et al. Microwave-assisted design of nanoporous graphene membrane for ultrafast and switchable organic solvent nanofiltration. Nat Commun 2023;14(1):901.
[3] Lin Y, Zhang Y, Dai Z, Peng X, Xue W, Zhang Y, Li N. In situ real-time quantitative characterization of nanofiltration membrane pore orientation for enhanced ion separation. Adv Mater 2025;37(28):e2500447.
[4] Wang H, Zhai Y, Li Y, Cao Y, Shi B, Li R, et al. Covalent organic framework membranes for efficient separation of monovalent cations. Nat Commun 2022;13(1):7123.
[5] Zhao J, Gleason KK. Solvent-less vapor-phase fabrication of membranes for sustainable separation processes. Engineering 2020;6(12):1432–42.
[6] Qiu F, Sun Y, Zhang Y, Liu H, Shao L, Huang Q. Electrospun PTFE nanofibrous composite membranes featuring a fiber network structure for organic solvent nanofiltration (OSN). Separ Purif Tech 2024;330:125416.
[7] Jin CG, Zhang WH, Tian N, Wu B, Yin MJ, An QF. Fabrication of coffee-ring nanostructured membranes for organic solvent nanofiltration. Angew Chem Int Ed Engl 2024;63(31):e202405891.
[8] Abdi ZG, Chen JC, Chung TS. Novel amino-beta cyclodextrin-based organic solvent nanofiltration membranes with fast and stable solvent transport. J Membr Sci 2024;689:122197.
[9] Fan H, He J, Heiranian M, Pan W, Li Y, Elimelech M. The physical basis for solvent flow in organic solvent nanofiltration. Sci Adv 2024;10(24):eado4332.
[10] Wu X, Ding M, Xu H, Yang W, Zhang K, Tian H, et al. Scalable Ti3C2Tx MXene interlayered forward osmosis membranes for enhanced water purification and organic solvent recovery. ACS Nano 2020;14(7):9125–35.
[11] Shi X, Li H, Chen T, Duan Y, Shi D, Kang C, et al. Selective liquid-phase molecular sieving via thin metal–organic framework membranes with topological defects. Nat Chem Eng 2024;1(7):483–93.
[12] Huang Z, Ling Zhao D, Shen L, Lin H, Chen C, Xu Y, et al. Mxenes for membrane separation: from fabrication strategies to advanced applications. Sci Bull 2024;69(1):125–40.
[13] Liu Z, Sun Y, Han H, Zhang Q, Li S, Zhang S. Microporous and functional group Co-designed polyesteramide membranes for efficient and broad-spectrum organic solvent nanofiltration. Adv Membr 2024;4:100098.
[14] Chen Y, Zhou X, Zhang T, Ge B, Niu QJ, Sun H. Rapid preparation of extremely highly permeable covalent organic polymers nanofiltration membranes for alcohol recovery via interfacial polymerization. Adv. Membr. 2024;4:100107.
[15] Liu ML, Sun YX, Tang Y, Fu ZJ, Wang Q, Wang ZY, et al. Graphene oxide hollow fiber membranes for solvent dehydration by nanofiltration. J Membr Sci 2023;683:121848.
[16] Liu ML, Guo JL, Japip S, Jia TZ, Shao DD, Zhang S, et al. One-step enhancement of solvent transport, stability and photocatalytic properties of graphene oxide/polyimide membranes with multifunctional cross-linkers. J Mater Chem A Mater Energy Sustain 2019;7(7):3170–8.
[17] Shi GM, Feng Y, Li B, Tham HM, Lai JY, Chung TS. Recent progress of organic solvent nanofiltration membranes. Prog Polym Sci 2021;123:101470.
[18] Soroko I, Bhole Y, Livingston AG. Environmentally friendly route for the preparation of solvent resistant polyimide nanofiltration membranes. Green Chem 2011;13(1):162–8.
[19] Lin J, Wang P, Bin J, Wang L. Achieving 1060 mW cm-2 with 0.6 mg cm-2 Pt loading based on imidazole-riched semi-interpenetrating proton exchange membrane at high-temperature fuel cells. Small 2024;20(29):e2311767.
[20] Hu J, Hardian R, Gede M, Holtzl T, Szekely G. Reversible crosslinking of polybenzimidazole-based organic solvent nanofiltration membranes using difunctional organic acids: toward sustainable crosslinking approaches. J Membr Sci 2022;648:120383.
[21] Zhang Y, Wang L, Li L, Wang H, Dong X, Pan Y, et al. Insight into the influences of thermal crosslinking on the transition from polyacrylonitrile based ultrafiltration membrane to organic solvent nanofiltration membrane. J Membr Sci 2023;679:121694.
[22] Xu Y, Yu S, Peng G, Sotto A, Ruan H, Shen J, et al. Novel crosslinked brominated polyphenylene oxide composite nanofiltration membranes with organic solvent permeability and swelling property. J Membr Sci 2021;620:118784.
[23] Montà-González G, Sancenón F, Martínez-Máñez R, Martí-Centelles V. Purely covalent molecular cages and containers for guest encapsulation. Chem Rev 2022;122(16):13636–708.
[24] Shimanovich U, Ruggeri FS, De Genst E, Adamcik J, Barros TP, Porter D, et al. Silk micrococoons for protein stabilisation and molecular encapsulation. Nat Commun 2017;8(1):15902.
[25] Chen C, Li H, Chen J, Li D, Chen W, Dong J, et al. Surface molecular encapsulation with cyclodextrin in promoting the activity and stability of fe single-atom catalyst for oxygen reduction reaction. Energy Environ Mater 2023;6(2):e12346.
[26] Wu H, Chen Y, Zhang L, Anamimoghadam O, Shen D, Liu Z, et al. A dynamic tetracationic macrocycle exhibiting photoswitchable molecular encapsulation. J Am Chem Soc 2019;141(3):1280–9.
[27] Xu H, Deng W, Shi L, Long J, Zhang Y, Xu L, et al. The role of the molecular encapsulation effect in stabilizing hydrogen-bond-rich gel-state lithium metal batteries. Angew Chem Int Ed Engl 2024;63(27):e202400032.
[28] Zhao LL, Cao XL, Luo C, Wang Q, Lu TD, Tang MJ, et al. Locking patterned carbon nanotube cages by nanofibrous mats to construct cucurbituril[n]-based ultrapermselective dye/salt separation membranes. Nano Lett 2023;23(10):4167–75.

[29] Wang Y, Liang RZ, Jia TZ, Cao XL, Wang Q, Cao JR, et al. Voltage-gated membranes incorporating cucurbit[n]uril molecular containers for molecular nano
[30] Xia QC, Yang WJ, Fan F, Ji M, Wang Y, Wang ZY, et al. Encapsulated polyethyleneimine enables synchronous nanostructure construction and In Situ functionalization of nanofiltration membranes. Nano Lett 2020;20(11):8185–92.
[31] Wang Y, Wang Q, Xia QC, Yang WJ, Wang XX, Sun SP, et al. Nanocapsule controlled interfacial polymerization finely tunes membrane surface charge for precise molecular sieving. Chem Eng J 2021;409:128198.
[32] Lu TD, Zhao LL, Yong WF, Wang Q, Duan L, Sun SP. Highly solvent-durable thin-film molecular sieve membranes with insoluble polyimide nanofibrous substrate. Chem Eng J 2021;409:128206.
[33] Hauschild MZ, Rosenbaum RK, Olsen SI. Life cycle assessment-theory and practice. Cham: Springer Cham; 2017.
[34] The International Organization for Standardization (ISO). ISO 14040:2006: Environmental management-life cycle assessment-principles and framework. ISO standard. Geneva: the International Organization for Standardization (ISO); 2006.
[35] The International Organization for Standardization (ISO). ISO 14044:2006: Environmental management-life cycle assessment-requirements and guidelines. Geneva: the International Organization for Standardization (ISO); 2006.
[36] Bulle C, Margni M, Patouillard L, Boulay AM, Bourgault G, De Bruille V, et al. IMPACT World+: a globally regionalized life cycle impact assessment method. Int J Life Cycle Assess 2019;24(9):1653–74.
[37] Demacsek C, Tange L, Reichenecker A, Altnau G. PolyStyreneLoop – the circular economy in action. IOP Conf Ser Earth Environ Sci 2019;323(1):012149.
[38] Liu Y, Xu J, Cao Z, Fu R, Zhou C, Wang Z, et al. Adsorption behavior and mechanism of Pb(II) and complex Cu(II) species by biowaste-derived char with amino functionalization. J Colloid Interface Sci 2020;559:215–25.
[39] Tang MJ, Liu ML, Wang DA, Shao DD, Wang HJ, Cui Z, et al. Precisely patterned nanostrand surface of cucurbituril[n]-based nanofiltration membranes for effective alcohol-water condensation. Nano Lett 2020;20(4):2717–23.
[40] Smolders CA, Reuvers AJ, Boom RM, Wienk IM. Microstructures in phase-inversion membranes. Part 1. Formation of macrovoids. J Membr Sci 1992;73(2–3):259–75.
[41] Zhang WH, Yin MJ, Zhao Q, Jin CG, Wang N, Ji S, et al. Graphene oxide membranes with stable porous structure for ultrafast water transport. Nat Nanotechnol 2021;16(3):337–43.
[42] Lee C, Lee S, Kang SW. Enhanced porous membrane fabrication using cellulose acetate and citric acid: improved structural integrity, thermal stability, and gas permeability. Carbohydr Polym 2024;324:121571.
[43] Peng LE, Yao Z, Yang Z, Guo H, Tang CY. Dissecting the role of substrate on the morphology and separation properties of thin film composite polyamide membranes: seeing is believing. Environ Sci Technol 2020;54(11):6978–86.
[44] Wang Q, He QY, Zhao LL, Wang Y, Fang R, Luo C, et al. Coaxial electrospun nanofibrous substrates with tunable wettability for constructing cucurbit[n]uril-embedded organic solvent nanofiltration membranes. Chem Eng J 2023;465:142880.
[45] Abdi ZG, Lai JY, Chung TS. Green modification of P84 co-polyimide with β-cyclodextrin for separation of dye/salt mixtures. Desalination 2023;549:116365.
[46] Goro MM, Abdi ZG, Weber M, Lai JY, Chung TS. Fabrication of sPPSU/P84 blend membranes for organic solvent nanofiltration with superior chemical stability and separation performance. Chem Eng J 2025;519:165501.

Declaration of Interest Statement

☒ The authors declare that they have no known competing financial interests or personal relationships that could have appeared to influence the work reported in this paper.

☐ The author is an Editorial Board Member/Editor-in-Chief/Associate Editor/Guest Editor for this journal and was not involved in the editorial review or the decision to publish this article.

☐ The authors declare the following financial interests/personal relationships which